Direct Measures of Large, Anisotropic Strains in Deformation of the Erythrocyte Cytoskeleton

James C-M. Lee*, Derek T. Wong#, and Dennis E. Discher*#§
Institute for Medicine and Engineering, Departments of *Chemical, §Mechanical, and #Bio-Engineering, University of Pennsylvania, Philadelphia, Pennsylvania 19104

ABSTRACT The erythrocyte's spectrin–actin membrane skeleton is directly shown to be capable of sustaining large, anisotropic strains. Photobleaching of an ~1-μm stripe in rhodamine phalloidin-labeled actin appears stable up to at least 37°C, and is used to demonstrate large in-surface stretching during elastic deformation of the skeleton. Principal extension or stretch ratios of at least ~200% and contractions down to ~40%, both referenced to an essentially undistorted cell, are visually demonstrated in micropipette-imposed deformation. Such anisotropic straining is seen to be consistent at a qualitative level with now classic analyses (Evans. 1973. *Biophys. J.* 13:941–954) and is generally nonhomogeneous though axisymmetric down to the submicron scale. Local, direct measurements of stretching prove quantitatively consistent (within ~10%) with integrated estimates that are based simply on a measured relative density distribution of actin. The measurements are also in close agreement with direct computation of mean spectrin chain extension in full statistical mechanical simulations of a coarse-grained network held in a micropipette. Finally, as a cell thermally fragments near ~48°C, the patterned photobleaching demonstrates a destructuring of the surface network in a process that is more readily attributable to transitions in spectrin than in F-actin.

INTRODUCTION

Thin networks of cytoskeletal protein form at many, if not all, mammalian cell membranes. A primary function of such structures would seem to be to resist membrane stretching or straining. The cytoskeletal network of the red cell provides a relatively simple system in which to study such mechanics. This membrane network is seen in electron microscopy to be a quasi-sixfold mesh in which the flexible protein spectrin cross-links short actin filaments (Byers and Branton, 1985). Defects and deficiencies in components of this meshwork certainly lead to easily fragmentable membranes and anemias of various sorts (Waugh and Agre, 1988; Mohandas and Evans, 1994). Spectrin is also found at the membrane of many other cells, including the cylindrically shaped outer hair cell from the inner ear. There it is seen to cross-link long actin filaments wrapped around the cell's circumference (Holley and Ashmore, 1990). The resulting anisotropic structure is detectably softer along the axial, i.e., spectrin, direction (Tolomeo et al., 1996) that coincides with the direction of sound transduction. Yet another example of a mesoscopically ordered membrane network is the nuclear envelope's assembly of lamin isoforms (Aebi et al., 1986). This nuclear lamina appears to be an approximately fourfold symmetric structure which stabilizes the nucleus against processes such as apoptosis (Dahm et al., 1998). For any of these noted examples of highly evolved and ordered networks, including the exceptionally well-characterized red cell membrane skeleton, the detailed local straining of the structure in deformation has remained largely unprobed. The present set of studies on the red cell's spectrin–actin membrane skeleton attempts to address this fundamental issue of molecularly specific deformation at a localized scale. Anisotropic microstretching of the network is directly revealed by combining micropipette aspiration with fluorescence patterned photobleaching (FPP) of a network-labeled cell (Fig. 1).

Micropipette aspiration techniques have been applied to red cells for several decades, and yet some key unanswered questions remain. Initial manipulation measurements (Rand and Burton, 1967) were advanced considerably by explicit connections to a spectrin network (Nicolson et al., 1971) and its stabilizing role in imparting a shear rigidity to the otherwise fluid plasma membrane (Evans, 1973a; Skalak et al., 1973; reviewed in Evans and Skalak, 1980; also, Mohandas and Evans, 1994). Importantly, a shear rigidity presumes a static state of shear or anisotropic strain; solids, by definition, can sustain such states, whereas fluids cannot. The first theoretical calculations of network shear, or anisotropic stretching, in micopipette aspiration were given by Evans (1973b) under the constraint, practical at the time, that the network deforms as an incompressible surface. A desire to put this constraint to the test motivated more recent fluorescence imaged microdeformation (FIMD) measurements of red cells in aspiration (Discher et al., 1994; Discher and Mohandas, 1996). The result has been a unified set of disparate component maps for membrane deformation. In particular, maps of the spectrin–actin skeleton correlate qualitatively as well as quantitatively with some of the properties expected of a sparse, approximately 2-dimensional (2D) network. For instance, under local compression and tension, the network reversibly sustains density varia-

Received for publication 16 September 1998 and in final form 27 April 1999.

Address reprint requests to Dr. Dennis Discher, Towne Bldg. 112, University of Pennsylvania, 220 S. 33rd St., Philadelphia, PA 19104-6315. Tel.: 215-898-4825; Fax: 215-573-6334; E-mail: discher@seas.upenn.edu.

0006-3495/99/08/853/12 $2.00

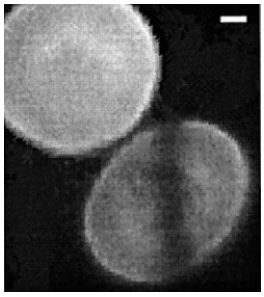

FIGURE 1 Flaccid red cell ghost at 23°C with a single line photobleached in rhodamine phalloidin-labeled actin by a focused laser beam. The pattern is stable for at least 30 min. The scale bar is ~1 μm.

tions that span a ten-fold range—in stark contrast to the density-invariance of the lipid bilayer that overlies the network. Based on such network density results, conservation of mass together with an assumption of axisymmetry have been invoked to argue that micropipette aspiration also leads to anisotropic stretching of the network. Local extensions as great as 250% in the axial direction of the micropipette have been shown to be simultaneously accompanied by contractions of at least 40% in the circumferential direction. Spectrin, based on its contour length (~200 nm) and an estimate of its in situ end-to-end length (~60–80 nm) (e.g., Byers and Branton, 1985), is certainly expected to be capable of sustaining such a large range of deformation. The various indirect proofs of anisotropic network stretching motivate a much more direct demonstration. Added impetus is provided by approximately whole-cell simulations of spectrin-like triangulated networks in micropipette deformation (Discher et al., 1998). These statistical mechanical computations have not only shown that spectrin is stretched, on average, as outlined above but also that network deformation is primarily confined to the aspirated projection of the cell membrane.

Complementary to FIMD is the well-established method of fluorescence recovery after photobleaching (FRAP) which, as generally used, monitors temporal, rather than spatial, changes of fluorophore density in a well-defined, photobleached pattern on a cell. Applied to the red cell transmembrane proteins band 3 (Golan and Veatch, 1980) and glycophorin C (Knowles, 1993), both FRAP and FIMD (Discher and Mohandas, 1996) have shown that a majority of these two components are immobilized by their linkages to the underlying skeleton. Both FRAP and FIMD have also demonstrated the in-surface fluidity of the lipid bilayer. Combining FRAP and FIMD by photobleaching a pattern on a moving or deforming cell and imaging the complex density field and pattern evolution in time and space has been more limited in application. With crawling keratocytes, much has been revealed about the detailed kinematics of how cytoskeletal actin convects and diffuses in relation to the substrate and boundary of this actively motile cell (Lee et al., 1993). With red cells moving in a shear field, the relative immobility of a fraction of band 3 was confirmed (Weaver et al., 1990). In application to the erythrocyte cytoskeleton deformed into a micropipette, FPP with imaging of states before and after deformation can directly and quantitatively test several key assumptions/conclusions made in prior analyses: 1) The network is a static, solid-like structure capable of sustaining strongly anisotropic or shear states. 2) Micropipette aspiration leads to a 2D, essentially axisymmetric deformation of the cytoskeleton. 3) Intensity maps of nonlipid components can be calibrated and physically interpreted as relative density maps by appealing to the incompressibility of the lipid bilayer and asserting that the lipid maps provide a measure of unity on a relative density scale.

The content of the paper is organized as follows. The next section highlights technical details of the experimental and computational methods used to understand local straining of the network by FPP of the labeled skeleton. Results are first briefly presented for coarsely defined limits of thermal stability (from ~23°C to ~50°C) of the network. Large-scale simulations of network photobleaching in deformation are subsequently used to introduce relevant metrics for cells deformed, bleached, and allowed to relax. Results are then presented for just such an experiment in which, first, a pattern is imposed on the aspirated projection of a cell held in a micropipette, and, after this, a second micropipette is used to extract the cell and suitably define a locally relaxed reference configuration. Subsequent discussions establish limits on the accuracy and interpretation of the direct and indirect methods. A final, concluding section provides a summary and points the way to future efforts.

MATERIALS AND METHODS

Labeling of membrane F-actin by rhodamine phalloidin

To label the internal skeletal network, red cells were reversibly permeabilized by cold, hypotonic lysis allowing molecules in the lysis buffer to diffuse into the permeabilized cell "ghost" and bind (Takakuwa et al. 1986; Lieber and Steck, 1989; Discher et al., 1995). Labeling of skeletal actin with rhodamine phalloidin was accomplished by first air-drying (5 μL 6.6 μM in MeOH) and then redissolving the phalloidin in (10–15 μL) cold lysis buffer (10 mM phosphate, pH 7.4 $\pm$ 0.1). Cold, packed red cells (5 μL) were added and, after 5 min, the suspension was made 100 mM in KCl, 1 mM in $MgCl_2$ and then warmed at 37°C for 20 to 60 min. Mechanical properties of the resealed membrane were not significantly altered by the labeling procedure as previously indicated (Discher and Mohandas, 1996), and a concentration-dependent edge-brightness had also indicated an apparent, in situ $K_a \sim 3 \times 10^6$ M (Discher et al., 1995) which is only slightly less than in vitro assays. Also shown was that rhodamine phalloidin does not fluorescently label unlysed cells. Labeled cell ghosts were either swollen, for micropipette manipulation, with phosphate buffered saline (PBS: lysis buffer plus 140 mM NaCl) diluted 2:1 with distilled water, or left flaccid in PBS. Bovine serum albumin (BSA) at 10 mg/mL was added to minimize adhesion to glass. For most of the studies conducted at higher than ambient temperature (~23°C), a closed stage (Focht Chamber System 2, Bioptechs, Butler, PA) was used with a claimed precision of $<$0.5°C up to 50°C. For several experiments performed with micropipettes at ~37°C, an open-sided, manipulation chamber was custom built; it had an estimated precision of $\pm$1°C.

Fluorescence pattern photobleaching and micropipette system

For FPP, a micropoint laser system (Photonic Instruments, Arlington Heights, IL) was coupled to the epi-illumination port of a Nikon TE300 epifluorescence microscope. A fiber optic from the system's pulsed nitrogen laser pumped coumarin 440 dye in the dye-cell resonator. The nonpolarized beam emitted from the resonator passed through focusing optics and a variable attenuator, allowing the beam intensity to be adjusted to minimize detectable damage to the membrane while also maintaining sufficient intensity to photobleach the rhodamine-labeled membrane. The beam emerged near the focal plane with near diffraction-limited dimensions. The 3 ns laser pulses typically were cycled at 20 Hz for several seconds to achieve bleaching that was detectable by imaging. Bleaching of fluorophores by pulsed dye laser systems has been reported relatively recently (Yuan and Axelrod, 1994) and appears partially predicated on a two-photon mechanism with irreversible bleaching persisting beyond a time of approximately ms for the rhodamine probe studied.

Excitation of rhodamine for imaging was accomplished through shuttered (Uniblitz, Vincent Associates, Rochester, NY) reflection into the epi-illumination port, and image collection occurred through the side-port of the microscope. A 10× lens magnified the image onto a Photometrics (Tucson, AZ) CH360 cooled and back-thinned charged coupled device (CCD) camera controlled with Image Pro (Silver Springs, MD) software. The excitation lamp shutter was synchronous with a second shutter exposing the CCD; the typical exposure time was set between 200–300 ms. The CCD is essentially the same as that employed in previous studies of FIMD (Discher et al., 1994). It is well-known for its linearity of intensity versus signal, and, at the emission wavelengths of rhodamine, it has a quantum efficiency in excess of 80%. A strain-free 60×, 1.4 NA objective lens was typically used with immersion oil having a refractive index of 1.52. The micropipette manipulation system was essentially the same as that described previously (Discher et al., 1994).

Polymerization and labeling of isolated actin for thermal stability test

Rabbit muscle G-actin was purchased as 99% pure in buffered solution from Cytoskeleton, Inc. (Denver, CO). G-actin was stored frozen at −70°C until use. To polymerize the actin, 16.7 μL 0.6 mg/mL G-actin solution was diluted by adding 58.3 μL deionized water followed by 25 μL buffer A (300 mM KCl, 10 mM $MgCl_2$, 40 mM PBS) to raise the ionic strength and initiate assembly of filaments. After incubation at room temperature for 10 min, the 100 μL 0.1 mg/mL F-actin was kept at 4°C. To label with rhodamine phalloidin (Sigma, St.Louis, MO), probe (45 μL 6.6 μM in MeOH) was air-dried and then redissolved in 100 μL of 0.1 mg/mL F-actin. The labeled F-actin was centrifuged at 80,000 × g for 1 hr at 4°C. Excess probe was removed with the supernatant, and the F-actin pellet was resuspended in buffer A. Sealed chambers for microscopy generally contained BSA to minimize adhesion between filaments and chamber.

Statistical mechanical simulation of discrete network models in deformation

Bead and tether models of the spectrin network (Boal, 1994; Boey et al., 1998) have recently been coarse-grained into triangulated surface lattices with nodal degrees of freedom. These enable full statistical mechanical simulations of spectrin network deformation (Discher et al., 1998). The approach taken is motivated by: 1) actual experiments, which suggest that micropipette-imposed network deformations are generally nonhomogeneous with very large strains in spectrin; 2) theoretical complexity for the large deformation responses of triangulated structures (Discher et al., 1997); and 3) the nontrivial entropic contribution of thermal fluctuations at the biologically-relevant temperature of ~300 K.

Briefly, in terms of triangle areas, A, and sides, l, the effective network Hamiltonian has the form

$$\mathcal{H}_{\text{net}} = \sum_{\text{triangles}} C/A + \sum_{\text{bonds}} V_{\text{eff}}(l). \quad (1)$$

The parameter C is essentially a virial coefficient estimated, a la Flory, by balancing steric pressure against chain elastic forces represented in $V_{\text{eff}}(l)$. The 3D bead and tether chains are thus replaced by two- and three-body 2D interactions, which effectively represent the many-segmented chains. At equilibrium, the balance of forces determines a mean chain length, l_o, which serves as a finite reference length. The chain elasticity term in Eq. 1 takes the form of an effective potential that interpolates between Gaussian and strong-stretching responses for worm-like chains (Marko and Siggia, 1995),

$$\beta V_{\text{eff}}(l) = (l_{\max}/4b)\xi^2(3 - 2\xi)/(1 - \xi), \quad (2)$$

where $\xi = l/l_{\max}$, and $l_{\max}$ is the maximum chain extension. Chain flexibility enters through the persistence length b and $\beta = 1/k_BT$. Chain extension or stretch is gauged by l_o, i.e., spectrin stretch $= l/l_o$.

For the micropipette deformations simulated in this paper, a fixed shape ensemble was used in which each node of the network undergoes thermal motion that is constrained to a specified surface embedded in three-space. Individual nodes are moved according to a Boltzmann weight involving $\mathcal{H}_{\text{net}}$. As shown previously (Discher et al., 1998), the coarse-grained network model that best fits published micropipette results on normal cells, including FIMD results, combines the above energetics with a precompression of the network, i.e., the surface-constrained network has an equilibrium area that is greater than the area of the cell. Further description of the model, including values for the parameters b and $l_{\max}$, may be found in the original reference (Discher et al., 1998). Simulation results for the present work were typically based on structures equilibrated for at least $>3 \times 10^6$ Monte Carlo steps, which took approximately one week on an R10000 processor of an SGI-Cray Origin 2000.

RESULTS

Time-temperature stability of a patterned, undeformed network

The time and temperature dependence of an ~1-μm line patterned on single cells was first examined in an effort to assess the stability of the network. Studies by others had shown that: 1) at temperatures in excess of ~40°C, spectrin in particular undergoes structural transitions that can lead to aggregation (Minetti et al., 1986; Lysko et al., 1981); and 2) the apparent shear modulus of the red cell persists but decreases with temperature (Waugh and Evans, 1979). The latter finding has been explained based on thermally activated dissociation of a fraction of spectrin cross-links from the network (Stokke et al., 1986). Based on bleached pattern stability (Fig. 2 *A*), however, such dissociation is likely to be very localized because, from ~23°C through 37°C, a pattern in the network is static for 30 min or more. For all five cells examined, intensity profiles through the line pattern were quantitatively unchanged for such periods at these temperatures. This obviously implies that, at optical length scales approaching the contour length of a spectrin tetramer (~200 nm; Byers and Branton, 1985), the red cell network appears solid-like, though softening via localized loss of network cross-links is certainly possible.

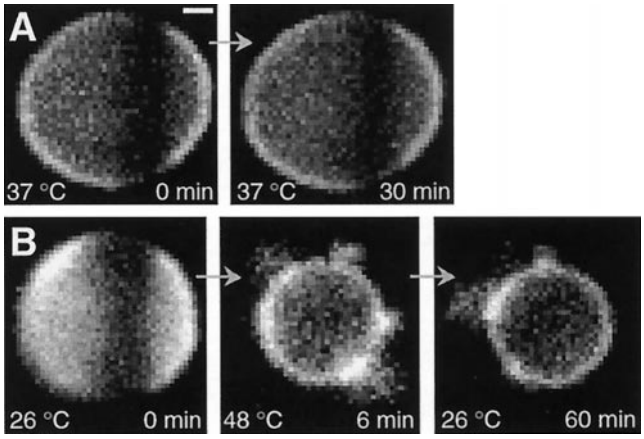

FIGURE 2 Thermal stability and transformation of representative red cells with membranes demarked by a photobleached line in rhodamine phalloidin-labeled actin. (*A*) The line on a flaccid cell was stable for at least ~30 min at 37°C. (*B*) A second cell with a line photobleached at 26°C, was rapidly heated to 48°C. After several minutes, membrane vesicles were shed. Although the actin remained peripheral, the line was no longer visible, suggesting fluidization of the network. The horizontal bar in the first panel is 1 μm.

Photobleached patterns do appear to dissipate within minutes (Fig. 2 *B*) in the temperature range where others have observed cell fragmentation (e.g., see Fig. 8 of Mohandas and Evans, 1994) and correlated to some extent with protein transitions. The labeling typically becomes nonhomogeneous on the membrane, but the evolved structures generally maintain a distinct edge-brightness as portions of the cell membrane are shed. Of six cells examined, the bleach pattern very clearly dissipated in all.

Thermal stability of a deformed, unpatterned network

Recent FIMD efforts of others (Artmann et al., 1998) have suggested that the network gradient, which forms in micropipette aspiration (Discher et al., 1994), is not visible above 28.3°C—notably at 37°C. Bleached patterns on undeformed cells were demonstrated in the present work, however, to be stable at 37°C; it therefore became important to try to reproduce the FIMD results of Artmann et al. (1998). The stress of aspiration could, in principle, accelerate the dissociation of spectrin from the network. Several rhodamine phalloidin-labeled red cells were thus examined by FIMD in an open-sided temperature chamber equilibrated at either 29°C or 38°C. Despite the reported findings of Artmann et al. (1998), in which a fluorescent, polyclonal antispectrin antibody was used, network actin was found in the present work to exhibit a strong, roughly linear gradient in density along the cylindrical projection at both 29°C and 38°C. Indeed, the difference between the relative densities of actin at the entrance and cap of the aspirated projection at these elevated temperatures was found in the present studies to be quantitatively indistinguishable (Fig. 3) from previous results gathered at ~23°C (Discher et al., 1994; Discher and Mohandas, 1996). The network thus seems stable and solid-like, albeit soft, at physiological temperature.

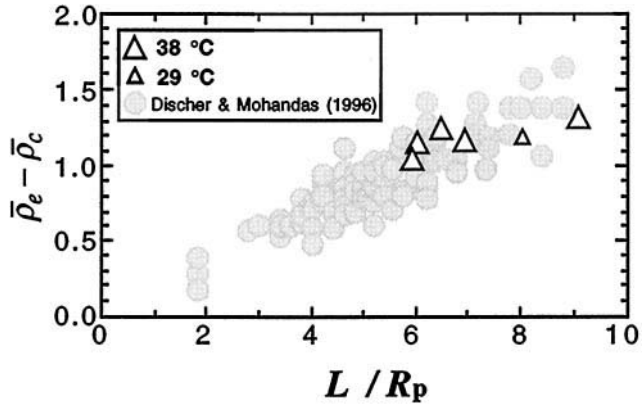

FIGURE 3 Difference between relative network densities at the entrance ($\bar{\rho}_e$) and cap ($\bar{\rho}_c$) of micropipette-aspirated projections of individual cells at either 29°C or 37°C. Network actin was labeled with rhodamine-phalloidin. Comparison is made to previous results at ~23°C for spectrin, actin, and protein 4.1 (Discher and Mohandas, 1996).

Time-temperature stability of isolated actin filaments

To provide a partial, molecular explanation for the time-temperature dependence of the cellular findings above, isolated actin was polymerized into filaments, labeled with the same rhodamine phalloidin probe, and examined under similar time-temperature conditions. Fig. 4 *A* shows isolated filaments freely suspended at 37°C for 30 min in a chamber containing BSA-PBS. Despite slightly increased thermal

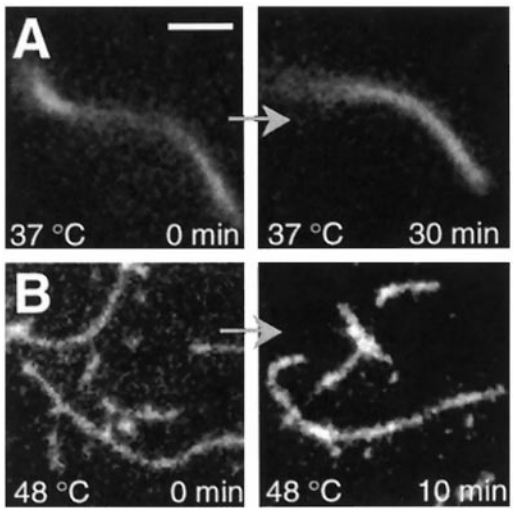

FIGURE 4 Time-temperature stability of isolated actin filaments labeled with rhodamine phalloidin. (*A*) The suspending solution contains BSA for minimizing adhesion of thermally fluctuating filaments to glass. (*B*) Filaments attached by poly-L-lysine to a coverslip; bulk suspended filaments indicated equivalent stability but were difficult to image due to strong thermal motion. The scale bar in the first panel is ~5 μm and applies to all images.

motions at elevated temperature, likely reflecting a softening of the bending rigidity rather than the controlled increase in k_BT, the filaments and, importantly, the phalloidin attachment were very clearly stable for extended periods, consistent with solution studies of binding (De La Cruz and Pollard, 1996). Similar results were found at 48°C, except that filament motion was overly dynamic; poly-L-lysine-coated coverslips were therefore used at these higher temperatures to partially immobilize the filaments for imaging. Clearly, what these single filament results suggest is that the cellular network results at 48°C (Fig. 2 *B*) reflect rearrangment of network components other than either F-actin or its labeling probe, rhodamine phalloidin. Further, these single filament results suggest some level of stability for probe labeling of networks under stress, albeit thermal stress.

Simulated photobleaching of a micropipette-deformed membrane network

To identify relevant metrics in the micropipette deformation of the erythrocyte cytoskeleton, statistical mechanical simulations were conducted on a coarse-grained spectrin network. A photobleached pattern of network tethers was formed in an aspirated configuration (Fig. 5) simply by applying a Gaussian probability for bleaching, $P_{\text{bleach}}(z')$. Each network tether represents the end-to-end vector of a convoluted spectrin chain, which, in Boey et al. (1998), would have had either 12 or 26 segments. The probability of a tether being bleached was assumed to depend on the distance from the center of the bleach. The standard deviation for the Gaussian bleach is simply chosen to approximate the focused beam width.

In these almost full-scale simulations, axisymmetry is not assumed for how the network conforms to the aspirated projection of specified radius (R_p) and length (L); as a consequence, relaxing the aspirated projection back into the surface of an essentially unstrained sphere of equal area does not, of necessity, yield a simple pattern. Nonetheless, the resultant pattern on a reference sphere closely approximates the expected finite-width circular pattern. The original Gaussian bleach remains quasi-Gaussian in this spherical state of the network. Further, one can readily view this state as a relatively unstrained reference state since a sphere is a close approximation of the true discocytic reference shape related through small surface strain eversions of the membrane's concave regions. Indeed, strains on spectrin tethers in the spherical state are less than 5% and are largely obscured by thermal fluctuations of the network. Moreover, if the sphered state, which defines a reference state in the simulations, were compared to a state in which a second projection is pulled at a position diametrically opposite to the first, then much of the spherical portion of cell outside the micropipette would continue to define a reasonable reference state, since strains are below the few percent level. Such a two-micropipette approach is, in fact, the approach employed in experiment; omitting the second extracting micropipette in the simulations appears to be of no significance.

Given the above, in both simulation and experiment, a number of direct but simple measures of network stretch are achievable. The first measure is provided by a ratio of the meridianal widths of the bleached region; dividing s^* in the deformed configuration (Fig. 5 *A*) by S_o^* in the reference configuration (Fig. 5 *B*) defines the extension ratio λ_1^*. This is clearly a local stretch measure in the axial direction that is averaged over an approximately micron-length scale. A coarser average in the same principal direction, $\langle\lambda_1\rangle$, takes advantage of the cell's axisymmetric configurations; $\langle\lambda_1\rangle = s/S_o$, is a ratio of a deformed curvilinear length, measured from the tip of the aspirated projection to one standard deviation from the bleach peak, and an undeformed curvilinear length, the arc measured off from the symmetry axis of the sphere to one standard deviation from the bleach peak in the sphered state. In the circumferential direction, denoted principal direction 2, one can readily estimate a contraction, a stretch ratio that should be less than one, corresponding to the network being radially confined by the micropipette radius. The most opportune point for such a measurement is at the curvilinear position s and is simply given by $\lambda_{2|s} = R_p/R_o$, where the undeformed length R_o is the radial distance to the symmetry axis of the network and roughly one standard deviation from the bleach peak in the spherical state. Finally, we note that pointwise conservation of mass for a 2D material, such as this network, relates the local relative density, $\bar{\rho}$, to local stretches in the axial and circumferential directions: $\bar{\rho} = 1/(\lambda_1\lambda_2)$ (e.g., Discher et al., 1994). Since $\lambda_{2|s}$ is a local measure, and since the $\bar{\rho}|_s$ can be reliably estimated from simple extrapolation of intensity into the bleached zone, the deformed state alone provides a simple method of calculating $\lambda_{1|s} = 1/(\bar{\rho}\lambda_2)|_s$.

Values for the above four network stretch measures, as thermally-simulated averages, are eventually discussed in relation to microscopic distributions of spectrin tether stretching, i.e., local histograms of l/l_o. More macroscopically, it should also be pointed out that the principal stretch or extension ratios above are related to Lagrangian strain measures: $E_{11} = \frac{1}{2}(\lambda_1^2 - 1)$, $E_{22} = \frac{1}{2}(\lambda_2^2 - 1)$, and $E_{12} = E_{21} = 0$ (e.g., Evans and Skalak, 1980). Only when $\lambda < 1 + (2\epsilon)^{1/2}$, where ϵ is a tolerable percent error, are these strain measures well approximated by infinitesimal strains expressible as a sum of linear displacement gradients (e.g., Landau and Lifshitz, 1986) and reducible to $(\lambda - 1)$ in principal directions. Since continuum strain measurements in biopolymer systems often have accuracies of order $\epsilon \sim$ 1–10% (as will be shown in the present case as well), a reasoned criteria for considering deformations as large is when $\lambda \gtrsim 1.5$. Finally, a definition for anisotropic deformation in terms of the principal λs is simply $\lambda_1 \neq \lambda_2$; and, as is intuitive, only solids and not fluids can sustain such states composed of shear for any extended period of time. More specifically, one can generally rotate to a local coordinate system on the surface that maximizes the off-diagonal, or shear strain components, and sets equal the on-diagonal, or dilatory strain components.

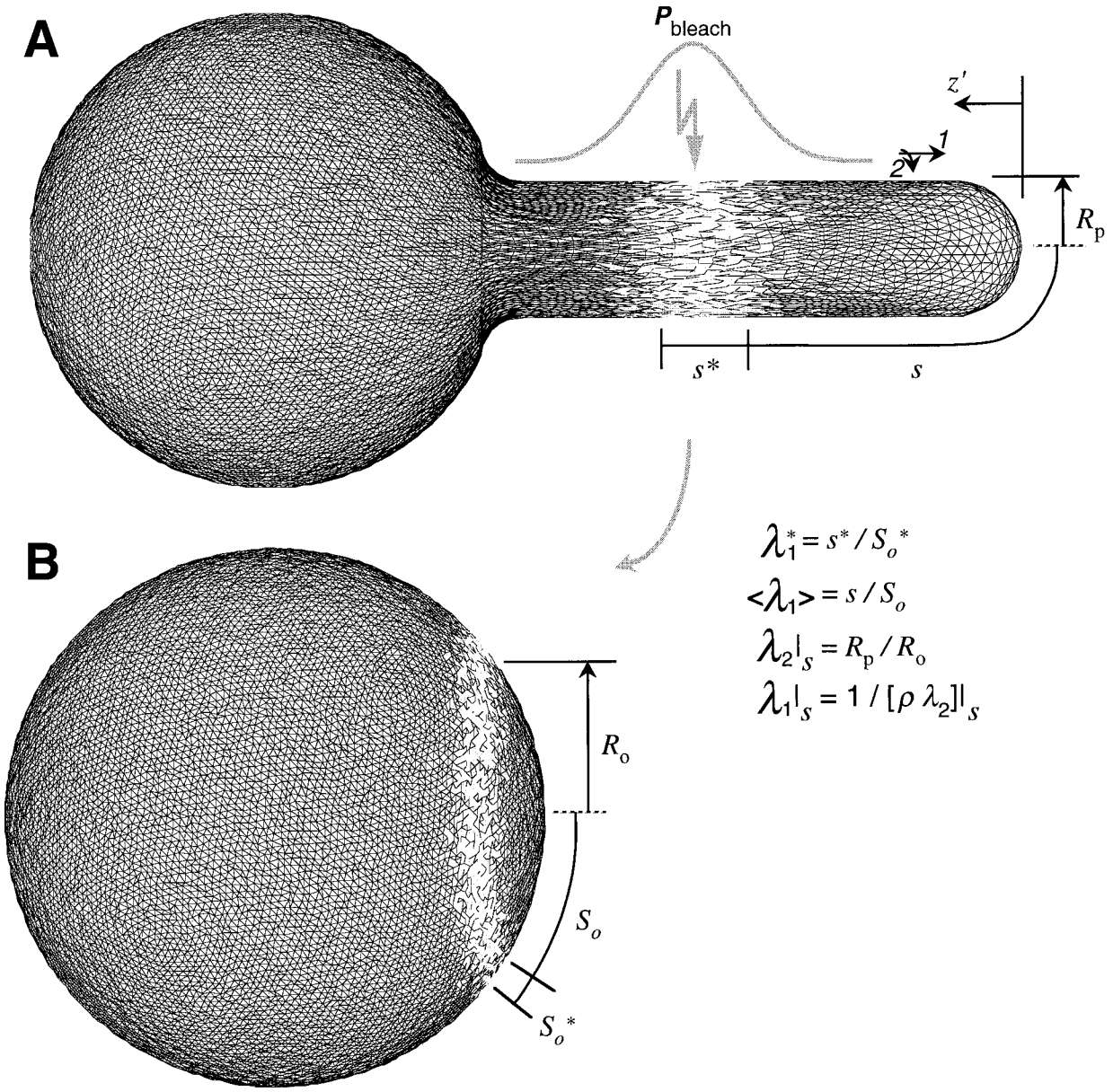

FIGURE 5 Simulated photobleach pattern in (*A*) a micropipette-deformed configuration and in (*B*) a reference-sphere configuration of a thermally-fluctuating spectrin network. The network consists of $\sim 5.5 \times 10^4$ spectrin tethers, which are nonlinear in their chain elasticity and which interact via excluded volume; the network nodes are in incessant motion on the specified surfaces, moving per a suitable Boltzmann weight. Tethers are bleached on the micropipette-aspirated projection according to where their midpoint lies in relation to representative parameters for the center ($s + \frac{1}{2}s^*$), height ($1 - I_{min}$), and root-variance ($\frac{1}{2}s^*$) of a Gaussian probability P_{bleach}. From both configurations, the various indicated lengths are used to estimate network stretching in the micropipette deformed state. On the sphere, the tethers have a mean reference length of $l_o = 75$ nm, whereas the projection geometry is specified in part by $R_p = 0.67$ μm, and $L/R_p = 8$.

Direct and indirect measures of microstretching of a deformed red cell

The demonstrated stability of the micropatterned network together with the above identifications provide sufficient basis for elucidating direct measures of stretch on an actual red cell. Toward this goal, a $\sim$1-μm line was controllably bleached on the projection of a micropipette-aspirated and rhodamine phalloidin-labeled red cell. A second micropipette, placed diametrically opposite to the first, was used to aspirate the photobleached cell back out of the first micropipette (Fig. 6). The transfer was performed within a minute of bleaching. The bleached line was tracked only with a single image taken of each state, to minimize possible photodamage effects in imaging (Discher et al., 1994). The bleached line tended to maintain its symmetry axis during the extraction process and invariably appeared, at least in side view to be quasicircular, consistent with axisymmetric deformation at a microscale.

To quantitatively characterize the photobleaching in subsequent image analysis, a Gaussian was fit to the bleached

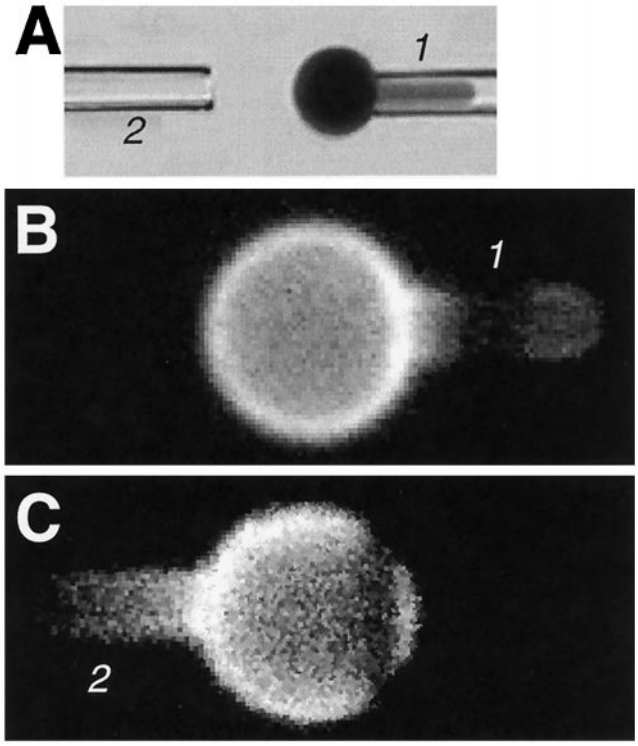

FIGURE 6 Images of the two-micropipette experiment used to measure the stretching on the micropipette aspirated projection. (*A*) Orientation of the two micropipettes just before transfer of a cell from the first to the second micropipette. (*B*) and (*C*) Representative fluorescence images of a rhodamine phalloidin-labeled cell ghost respectively held and bleached in the first micropipette and then extracted and held in the second micropipette. The micropipette diameter in these latter images is ~1.6 μm.

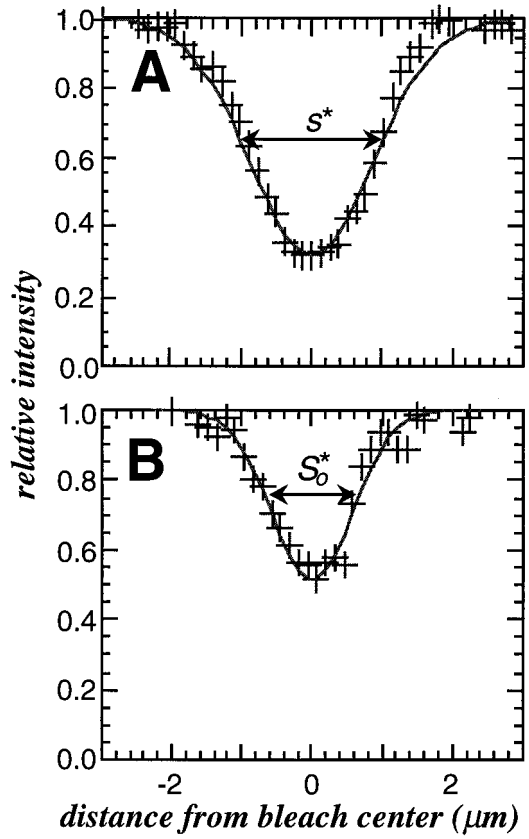

FIGURE 7 Gaussian fits of bleach profiles in a representative experiment (*crosses*). (*A*) Bleach profile on the projection after subtracting away a polynomial interpolation of the network density gradient upon which the bleaching beam acts. (*B*) The corresponding profile on the spherical contour of membrane outside the second micropipette.

pattern both along the projection in the aspirated state (Fig. 7 *A*) and along the outer membrane contour of the sphere in the second or undeformed reference state (Fig. 7 *B*). The depth of the bleach, I_{min}, in the aspirated states ranged between 0.16 to 0.42, corresponding to more and less bleaching, respectively. Because photobleaching has been noted to be a factor in material alteration of the network (Discher et al., 1994), it was considered important to minimize the bleach depth while still allowing detectable contrast of the bleach pattern in state 2. The standard deviations of the fits illustrated in Fig. 7 immediately reveal stretching of the network in the aspirated state since $s^* > S_o^*$. One standard deviation from the peak also demarks a relatively well-defined and minimally bleached material point in the image to which stretch measurements can be made.

Direct measurements of microstretching from such patterned bleaching experiments are tabulated for an approximately twofold range of projection lengths in Table 1. Various measures of λ_1 are consistently seen in this table to be much greater than λ_2. Local, anisotropic deformations are therefore directly revealed in micropipette-aspirated red cell membranes. Moreover, the various λ_1s have values of 2 within 10–20%, thus demonstrating very large network straining at least in the region of the projection one-third to one-half of the length from the tip. The quantity s^* reflects the mean of two separate fits of measures made at the two outermost edges of a projection's bleach pattern; the λ_1s are calculated from suitably paired bleach patterns and differ by less than ~2% within a pair. It is generally seen that the meridional stretching of the bleach pattern, λ_1^*, is greater than or equal to the average stretch, $\langle\lambda_1\rangle$, of unbleached network between the projection tip and the pattern; the relative difference does not exceed ~25% and is typically 5–10%. The more locally related quantities, λ_1^* and $\lambda_{1|s}$, are also very similar with relative differences not exceeding ~12%. Note that $\lambda_{1|s}$ is determined by estimating the relative density, $\bar{\rho}|_s$ (Table 2) via extrapolation through the

TABLE 1 Direct measures of stretching on micropipette deformed projections

Cell No.	L/R_p	R_p (μm)	R_s/R_p	s^*/R_p	s/R_p	λ_1^*	$\langle\lambda_1\rangle$	$\lambda_{2\|s}$	$\lambda_{1\|s}$
1	7.1	0.84	3.2	2.8	3.2	1.9	1.7	0.56	2.1
2	9.9	0.90	2.4	2.4	5.3	1.8	1.8	0.49	2.0
3	11	0.77	3.2	3.3	3.6	2.0	1.8	0.53	1.8
4	11	0.97	2.4	2.5	4.1	2.1	1.6	0.45	2.0
5	12	0.71	3.4	4.3	6.0	1.9	1.8	0.38	1.9
6	15	0.71	2.7	3.7	6.3	1.7	1.6	0.40	1.5

TABLE 2 Stretch measures for cells of Table 1 as obtained from the integration of $\bar{\rho}(z')$ (Eq. 3)

Cell No.	$\bar{\rho}_{\|s}$	λ_1^*	$\langle\lambda_1\rangle$	$\lambda_{2\|s}$	$\lambda_{1\|s}$
1	0.86	2.3	1.6	0.59	2.0
2	1.02	2.1	1.8	0.48	2.0
3	1.04	2.3	1.8	0.51	1.9
4	1.10	2.2	1.6	0.47	1.9
5	1.39	2.1	1.8	0.36	2.0
6	1.64	1.8	1.9	0.38	1.6

bleached stripe. Finally, the circumferential stretch ratio local to the bleached pattern, $\lambda_{2|s}$, is consistently less than unity, simply reflecting the contraction that occurs as a disk of network is physically constrained into the smaller-circumference micropipette.

As introduced in earlier studies of FIMD, an indirect estimate of microstretching is obtainable from the relative density field. In essence, this second independent measure relies on the accuracy of converting the intensity distribution of rhodamine phalloidin-labeled F-actin along the projection to a relative surface density profile. This conversion was achieved by recognizing that the (uniform) lipid density profile measured previously provided a measure of 1.0 ($\pm$10%) on a generic scale for relative density (Discher et al., 1994). Along the projection, up through an extrapolation into the bleached zone, λ_2 was further calculated from an expression based on the lipid-calibrated $\bar{\rho}_{net}$, together with mass conservation and an assumption of axisymmetric deformation (Discher and Mohandas, 1996),

$$\lambda_2(z') = \frac{r(z')}{R_p}\left\{\left(\frac{R_{s2}}{R_p}\right)^2 - \left[\left(\frac{R_{s2}}{R_p}\right) - \left(\frac{1}{R_{s2}}\right)_{tip}\int^{z'} \bar{\rho}_{net}\, dz'\right]^2\right\}^{-1/2}. \quad (3)$$

The upper limit on the integral, z', is the axial distance from the tip (Fig. 5). The radial distance from the axis of symmetry is, for $z' \geq R_p$, given by $r(z') = R_p$, and the reference sphere has a radius given by R_{s2} corresponding to the radius of the spherical segment outside the micropipette in state 2. Fig. 8 provides an illustration of the relative density and stretch fields, including λ_1 calculated from the previously identified local form for conservation of mass, $\lambda_1 = 1/(\bar{\rho}\lambda_2)$. Apparent again is the anisotropic straining of the network evident in $\lambda_1 > \lambda_2$, a disproportionality that grows away from the projection tip. At the tip, the principal stretches are equal, as dictated by symmetry.

The microdeformation results of the same deformed cells listed in Table 1 were analyzed by the indirect method using Eq. 3. The results are tabulated in Table 2. The quantity λ_1^* in Table 2 is computed by averaging the λ_1 profile (e.g., Fig. 8) over the interval defined by s^*. As suggested by the rough monotonic increases generally seen in the λ_1 profiles, λ_1^* is consistently greater than the other measures of λ_1 in Table 2; likewise, $\lambda_{1|s}$ typically exceeds $\langle\lambda_1\rangle$. Also, as pointed out for Table 1, the circumferential stretches are again consistently less than 1, indicating contraction in deformation.

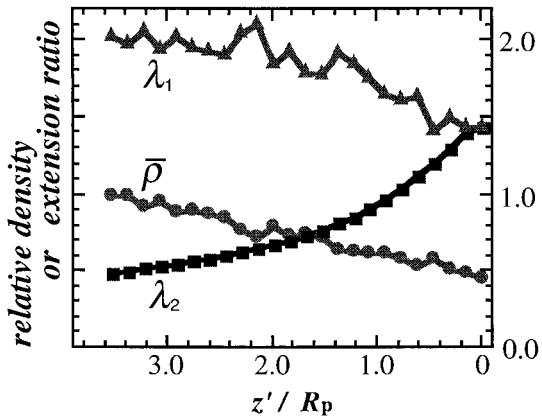

FIGURE 8 Estimation of stretch fields up to the center of the bleached region as determined from experimental relative density field. The projection length and micropipette radius for this aspirated cell were, respectively, $L/R_p = 8.5$ and $R_p = 0.71$ μm.

A comparison of direct and indirect measures of Tables 1 and 2, respectively, shows the largest discrepancy, up to ~20%, in the listings of λ_1^*. It is possible that the difference is physical and arises with photodamage in bleaching, a proposition supported by the fact that the direct method always yields a stretch measure that is lower than that estimated indirectly from the unbleached intensity. However, there was no definitive correlation between either the bleaching depth or width (I_{min} or s^*) and the relative difference between comparable stretch determinations. Furthermore, determinations of $\langle\lambda_1\rangle$ do not explicitly involve photobleached regions of membrane and also differ somewhat between the direct and indirect measures. Generally, however, the relative agreement among the various measures is between 5% and 15%, with better than 10% agreement being consistently achieved with the local measures $\lambda_{2|s}$ and the relative density-derived quantity $\lambda_{1|s}$. This level of accuracy is, it should be recalled, also claimed for the determinations of the relative density profiles that form the experimental basis of Table 2. These independent determinations, direct and indirect, therefore indicate a high degree of confidence in experimental measures of large, anisotropic strain as assessed by both the direct and indirect methods.

DISCUSSION

Solid-like network at sub-micron length scales up to 37°C

Determinations of stable, stretched states are certainly well founded in the solid-like behavior evident in the time-temperature studies. Indeed, the time-temperature dependence of photobleached patterns in nonaspirated erythrocyte ghosts demonstrated that, up to 37°C, but not near 48°C, the network appears solid-like. That is, diffusion of network actin is undetectable. This certainly is consistent with what

is probably a better phenomenological assessment of solidity at elevated temperature: the persistence of a measurable effective shear modulus (Waugh and Evans, 1979). Indeed, with a large collection of data showing that the spectrin–actin network is a central contributor to the molecular basis of red cell shear elasticity (reviewed in Mohandas and Evans, 1994), the solid-like behavior of the network seen here is readily anticipated. However, Waugh and Evans (1979) also documented a softening of the shear rigidity, a finding that argues against the prevailing idea (Evans and La Celle, 1975; Evans and Skalak, 1980) that red cell elasticity has a basis in spectrin chain entropy. An explanation for this softening is, in part, provided by a reduction in network connectivity at high temperature (Stokke et al., 1986); that is, disconnected spectrin dimers are favored over cross-linking spectrn tetramers. Qualitatively consistent with this, the observed thermal stability of (rhodamine-labeled) actin filaments (Fig. 3), suggests that network rearrangments should indeed be spectrin-based. Thus denoting the total number of spectrin cross-links by N_c, the calculations of Stokke et al. (1986) yield the fractional change in cross-link number as $(\Delta N_c/N_c) \approx \phi(\Delta T/T)$. The factor ϕ is determined from the temperature-dependent spectrin association constant (in vitro), K_a (Ungewickell and Gratzer, 1978), an assumed network thickness of 20 nm, and the spectrin tetramer concentration $[S]$ at the membrane when all of the spectrin is tetrameric; specifically, $\phi = T(\partial \ln K_a/\partial T)/(1 + 16K_a[S])^{1/2} \approx -1$ to -3. Thus, with an increase in temperature from 23 to 37°C, it is estimated that $(\Delta N_c/N_c) \approx -0.05$ to -0.15. The present experimental results indicate that such softening rearrangements must be very localized, essentially undetectable at optical scales (~250 nm). With such a ΔT, a triangulated network structure at 23°C may lose, in the extreme, one of six internodal cross-links.

Based on the above Δ-cross-linking model of Stokke et al., an increase in temperature from 23 to 48°C would essentially decrease the number of cross-links by a factor of two: $(\Delta N_c/N_c) \approx -0.1$ to -0.3. The latter, extreme value approaches that required for a vanishing shear modulus at a rigidity percolation limit of $(\Delta N_c/N_c) \approx -0.33$ in a stress-free triangular lattice of Hookean springs (Feng et al., 1985). Despite the possible appeal of this, however, such a model is likely to be too idealized; additional softening mechanisms, such as protein denaturation, are very likely to be operative in the high-temperature (i.e., 48°C) reconstructions of the network evident in Fig. 2 *B*.

The Δ-cross-linking model does not provide immediate insight into how N_c might be affected by local stresses in the network. Experimentally, however, even under the stress of micropipette aspiration, the actin-labeled network appears to be stable up to 37°C (Fig. 3). This apparent difference with the findings of Artmann et al. (1998), which suggested a thermally-driven dissipation of the aspirated network gradient, might be due to differences in experimental technique. First, in the studies of Artmann et al., labeling of spectrin is reportedly achieved with a polyclonal antibody. Such a probe mixture could very well have a weak, temperature- and conformation-sensitive affinity for spectrin. Suggestive of this: all four images in Artmann et al. exhibit almost no edge-brightness when compared to either the present results with rhodamine-phalloidin-labeled actin or previous results with fluorescein-phalloidin-labeled actin, fluorescein-protein 4.1, or fluoresceinated anti-αII spectrin antibody (Discher et al., 1994, 1995; Discher and Mohandas, 1996). Further, without any measure of labeling concentration or affinity provided by Artmann et al., it seems very possible that excessive concentrations of probe were used. The lack of edge-brightness certainly indicates that a large fraction of probe is not network bound and is simply entrapped in the ghost; it is particularly worrisome that the edge-brightness in the intensity profiles is least apparent at high temperature. Second, brightfield images of aspirated cells in Artmann et al., show that the micropipette is held at a variable angle with respect to the focal plane, in contrast to the in-plane orientation illustrated in Fig. 6 of this work. A non-zero angle can introduce an apparent gradient where there is none or, possibly, make a gradient appear to vanish. In this regard, it is noteworthy that the intensity profiles for low temperature in Artmann et al. (1998) do not resemble in any quantitative manner the data that are cited for comparison (Discher et al., 1994).

Two additional ideas, in combination with conclusions from the Δ-cross-linking model of Stokke et al. (1986), suggest that the gradient in network density on the aspirated projection should not change from 23 to 37°C. First, this gradient can be thought of most simply as reflecting a ratio of bulk: shear elastic moduli for a 2D network (Discher et al., 1994, 1998). Second, rigidity percolation results (Feng et al., 1985) indicate that this same ratio of elastic constants is essentially invariant at cross-link densities well above percolation. Therefore, since an increase in temperature from 23 to 37°C yields a structure that is estimated to be well above the percolation threshold, the observed gradient should not change.

In sum, we find no clear evidence for a temperature effect, up to 37°C, on the gradient response of the network in aspiration.

Stretch measures in a simulated network: Intracomparisons

To clarify both the accuracy and detailed meaning of the experimental strain determinations, a set of pure simulation results was analyzed by the various algorithms for stretch. The direct approach with a Gaussian bleach pattern was simulated as shown in Fig. 5, but, to illustrate the extremes, patterns were located either close to the projection tip or very near the entrance to the micropipette, rather than in the vicinity of the middle of the projection. The bleach positions and widths in the deformed state along with direct determinations of the various λ are tabulated in Fig. 9 *A*. Also tabulated are the same quantities determined by Eq. 3. This

A

bleach position	*Direct Measure*		*Integration of* $\bar{\rho}(z')$		*Stretch Distributions*
$z'/R_p =$ 2.5 ± 1	λ_1^*	2.00	λ_1^*	1.93	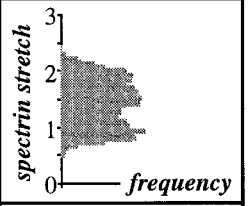
	$\langle\lambda_1\rangle$	1.75	$\langle\lambda_1\rangle$	1.87	
	$\lambda_1\|_s$	1.95	$\lambda_1\|_s$	1.97	
	$\lambda_2\|_s$	0.75	$\lambda_2\|_s$	0.76	
$z'/R_p =$ 7.7 ± 1	λ_1^*	--	λ_1^*	--	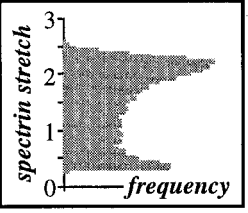
	$\langle\lambda_1\rangle$	2.10	$\langle\lambda_1\rangle$	2.15	
	$\lambda_1\|_s$	2.40	$\lambda_1\|_s$	2.40	
	$\lambda_2\|_s$	0.32	$\lambda_2\|_s$	0.32	

B

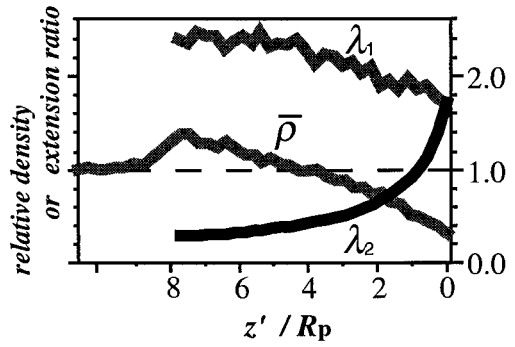

FIGURE 9 Measures of stretching of the spectrin network in simulations of micropipette aspiration. (*A*) Comparison of the direct and indirect methods of stretch determination at two positions along the projection and specified by the center and variance of the bleach. The last column indicates the thermally-averaged distributions of molecular stretching of spectrin in a narrow bin ($R_p/4$) near the center of the bleach. (*B*) Thermally averaged relative density and stretch profiles computed along the entire projection from the tip to the micropipette entrance using Eq. 3. The simulated cell has a projection length fixed at $L/R_p = 8$.

employs, it will be recalled, only an integration of the relative density field as based on conservation of mass and axisymmetry. A thermally averaged relative density profile along the computational projection is illustrated in Fig. 9 *B* together with the calculated stretch fields. Where necessary, the λs tabulated in Fig. 9 *A* employ simple spatial averaging, such as for $\langle\lambda_1\rangle$. The only allowance for optics in this second analysis is in setting the binning interval along the z'-direction at a fraction of the wavelength of light (~175 nm). The level of agreement between the direct and the indirect measures of stretch, when applied to the simulated model, is consistently better than ~6%. Experimentation comes within a factor of two to three of this theoretical limit of accuracy.

One feature of note in the relative density distributions and the complementary stretch fields in both Figs. 8 and 9 *B* is the roughness. This seems, in part, to reflect the underlying substructure tempered by its thermally-averaged motion. Indeed, at a more microscopic level, distributions of spectrin stretch (*last column* of Fig. 9 *A*) clearly provide a basis for the λs while also appearing much richer. For instance, in an optical bin near the entrance of the micropipette (at $z'/R_p = 7.7$), the distribution of spectrin stretch, l/l_o, is strongly bimodal with broad peaks centered near 2.25 and 0.35; these values differ by less than 10% from the computed tabulations for λ_1 and λ_2 at this position. Furthermore, these differences are smaller than the apparent widths of peaks at their respective bases, which easily span more than 25% of the peak stretch values. Closer to the projection tip ($z'/R_p = 2.5$), the bimodal distribution just begins to emerge from a single broad peak at the very tip where, in thermal rather than spatial averaging, $\langle\lambda_1\rangle \approx \langle\lambda_2\rangle$ (see Fig. 7 in Discher et al., 1998). Again, the peaks in the distributions roughly correspond to the tabulated λs. In both distributions, moreover, a large number of spectrin tethers distribute between the two peaks, and these intermediate chain extensions necessarily modulate the effective mean stretching by contributing to the relative density more so than do extremes in stretch. From one finite optical bin to the next along the projection, chains repopulate the stretch peaks and mid-distribution in a spatially dependent and necessarily incremental fashion. This follows from a comparison of scales: an optical resolution of ~0.2 μm is small compared to the ~0.1-μm length scale of the triangulated spectrin structure stretched and constrained to the projection. More explicitly, provided any sort of regular network triangulation, the ~±10% variation in λ_1 (≈ 2) about otherwise smooth behavior suggests that a fraction of actin nodes or chains, extended from ~75 to ~150 nm, are counted in one optical bin and pulled out of a neighboring bin. To emphasize the implicit discreteness of structure studied in FIMD of a real cell, an estimate of the number of actin protofilaments contributing to an optical bin of width 0.25 μm is ~(3×10^4 actin protofilaments per cell) ($2\pi R_p \times 0.25$

μm)/135 μm^2 ~ 250 filaments, which assumes a normal cell area and a relative density ~1. Modulations of ±10% in kinematic quantities thus involve only ~25 actin nodes!

Based on the consistency between experimental and theoretical measures of strain in the range of micropipette sizes used, what is generally true is that the maximum λ_1 and minimum λ_2 occur near the micropipette entrance and increase and decrease, respectively, with projection length. These trends are most fully appreciated from the indirect method of density profile integration as illustrated in Figs. 8 and 9 *B* and as introduced elsewhere (Discher and Mohandas, 1996). At a microscopic level, λ_1 and λ_2 closely correspond to the local means in cross-sectional distributions of spectrin chain stretching. Such distributions also reveal a large degree of locally heterogeneous deformation, which is perhaps most relevant to molecular theories of overstretched failure of the spectrin network.

CONCLUSION

The findings here quantitatively define molecular redistributions for both a set of specific membrane molecules (all membrane actin) and a small subset of the same molecules (a physically demarked subset of membrane actin). FIMD, as previously applied, yields local relative densities, which, when integrated assuming detailed axisymmetry, further reveal network stretches or strains that are within ~10% of direct and novel measurements made by FPP. A primary hypothesis regarding spectrin–actin network deformation is thus now established: large anisotropic strains are definitively sustainable. Further time-temperature studies substantiate the requisite solid-like character of the network.

Analyses of the large-scale simulation results for the spectrin network prove consistent with the experimental findings and indicate that the overall accuracy of experimental determinations is close to the theoretical limit. Importantly, because the experiments clearly show that relative density gradients provide sufficient description of network deformation, agreement between simulated and experimental relative density profiles (Discher et al., 1998) is a very reasonable test of model accuracy. However, in the spectrin stretch distributions and profile roughness, the simulations also point to additional structure to be revealed in deformation. It may, for instance, be possible, after computations on more structures, to clarify network connectivity through reversible deformation of an intact membrane with averaged density correlation functions along the projection. In avoiding the myriad of preparation artifacts of electron microscopy, such an approach could prove especially useful in elucidating red cell pathologies such as spectrin deficiencies, as well as the distinct spectrin–actin lattice of the outer hair cell membrane, or the remarkable square lattice of the nuclear lamina.

Professor David Boal is gratefully acknowledged for his many contributions to the foundations of the model network simulations. Professor Evan Evans is gratefully acknowledged for many prescient insights into the kinematics of red cell deformation. Thanks to Brian Helmke of the University of Pennsylvania's Institute for Medicine and Engineering for loan of the controlled-temperature stage. This work was supported in part by the Whitaker Foundation and National Institutes of Health R01-HL62352–01.

REFERENCES

Aebi, U., J. Cohn, L. Buhle, and L. Gerace. 1986. The nuclear lamina is a meshwork of intermediate-type filaments. *Nature*. 323:560–564.

Artmann, G. M., C. Kelemen, D. Porst, G. Büldt, and S. Chien. 1998. Temperature transitions of protein properties in human red blood cells. *Biophys. J.* 75:3179–3183.

Boal, D. H. 1994. Computer simulation of a model network for the erythrocyte cytoskeleton. *Biophys. J.* 67:521–529.

Boey, S. K., D. H. Boal, and D. E. Discher. 1998. Simulations of the erythrocyte cytoskeleton at large deformation. I. Microscopic models. *Biophys. J.* 75:1573–1583.

Byers, T. J., and D. Branton. 1985. Visualization of the protein associations in the erythrocyte membrane skeleton. *Proc. Natl. Acad. Sci. USA*. 82:6153–6157.

Dahm, R., C. Gribbon, R. A. Quinlan, and A. R. Prescott. 1998. Changes in the nucleolar and coiled body compartments precede lamina and chromatin reorganization during fibre cell denucleation in the bovine lens. *Eur. J. Cell Biol.* 75(3):237–246.

De La Cruz, E. M., and T. D. Pollard. 1996. Kinetics and thermodynamics of phalloidin binding to actin filaments from three divergent species. *Biochemistry*. 35:14054–14061.

Discher, D. E., N. Mohandas, and E. A. Evans. 1994. Molecular maps of red cell deformation: hidden elasticity and in situ connectivity. *Science*. 266:1032–1035.

Discher, D. E., R. Winardi, P. O. Schischmanoff, M. Parra, J. G. Conboy, and N. Mohandas. 1995. Mechanochemistry of protein 4.1′s spectin–actin binding domain: ternary complex interactions, membrane binding, network integration, structural strengthening. *J. Cell Biol.* 130: 897–907.

Discher, D. E., and N. Mohandas. 1996. Kinematics of red cell aspiration by fluorescence-imaged microdeformation. *Biophys. J.* 71:1680–1694.

Discher, D. E., D. H. Boal, and S. K. Boey. 1997. Phase transitions and anisotropic responses of planar triangular nets under large deformation. *Phys. Rev. E.* 55:4762–4772.

Discher, D. E., D. H. Boal, and S. K. Boey. 1998. Simulations of the erythrocyte cytoskeleton at large deformation. II. Micropipette aspiration. *Biophys. J.* 75:1584–1597.

Evans, E. A. 1973a. A new material concept for the red cell membrane. *Biophys. J.* 13:926–940.

Evans, E. A. 1973b. New membrane concept applied to the analysis of fluid shear- and micropipette-deformed red blood cells. *Biophys. J.* 13:941–954.

Evans, E. A., and P. L. La Celle. 1975. Intrinsic material properties of the erythrocyte membrane indicated by mechanical analysis of deformation. *Blood*. 45:29–43.

Evans, E. A., and R. Skalak. 1980. Mechanics and Thermodynamics of Biomembranes. CRC Press, Boca Raton, FL.

Feng, S., M. F. Thorpe, and E. Garboczi. 1985. Effective medium theory of percolation on central-force elastic networks. *Phys. Rev. B.* 31: 276–280.

Golan, D. E., and W. Veatch. 1980. Lateral mobility of band 3 in the human erythrocyte membrane studied by fluorescence photobleaching recovery: evidence for control by cytoskeletal interactions. *Proc. Nat. Acad. Sci. USA.* 77:2537–2541.

Holley, M. C., and J. F. Ashmore. 1990. Spectrin, actin and the structure of the cortical lattice in mammalian cochlear outer hair cells. *J. Cell Sci.* 96:283–291.

Knowles, D. W. 1993. Ph.D. Dissertation, University of British Columbia, Vancouver, BC, Canada.

Landau, L. D., and E. M. Lifshitz. 1986. Theory of Elasticity. 3rd ed. Pergamon Press, Oxford, UK.

Lee, J., A. Ishihara, J. A. Theriot, and K. Jacobson. 1993. Principles of locomotion for simple-shaped cells. *Nature*. 362:167–171

Lieber, M. R., and T. L. Steck. 1989. Hemolytic holes in human erythrocyte membrane ghosts. *Methods Enzymol.* 173:356–367.

Lysko, K. A., R. Carlson, R. Taverna, J. Snow, and J. F. Brandts. 1981. Protein involvement in structural transition of erythrocyte ghosts. Use of thermal gel analysis to detect protein aggregation. *Biochemistry*. 20: 5570–5576.

Marchesi, V. T. 1974. Isolation of spectrin from erythrocyte membranes. *Methods Enzymol.* 32:275–277.

Marko, J. F., and E. D. Siggia. 1995. Stretching DNA. *Macromolecules*. 28:8759–8770.

Minetti, M., M. Ceccarini, A. M. Di Stasi, T. C. Petrucci, and V. T. Marchesi. 1986. Spectrin involvement in a 40 degrees C structural transition of the red blood cell membrane. *J. Cell. Biochem.* 30:361–370.

Mohandas, N., and E. Evans. 1994. Mechanical properties of the red cell membrane in relation to molecular structure and genetic defects. *Ann. Rev. Biophys. Biomol. Struct.* 23:787–818.

Nicolson, G. L., V. T. Marchesi, and S. J. Singer. 1971. The localization of spectrin on the inner surface of human red blood cell membranes by ferritin-conjugated antibodies. *J. Cell Biol.* 51:265–272.

Rand, R. P., and A. C. Burton. 1964. Mechanical properties of the red cell membrane. I. Membrane stiffness and intracellular pressure. *Biophys. J.* 4:115–132.

Skalak, R., A. Tozeren, R. P. Zarda, and S. Chien. 1973. Strain energy function of red blood cell membranes. *Biophys. J.* 13:245–264.

Stokke, B. T., A. Mikkelsen, and A. Elgsaeter. 1986. The human erythrocyte membrane skeleton may be an ionic gel. I. Membrane mechanochemical properties. *Eur. Biophys. J.* 13:203–218.

Takakuwa, Y., G. Tchernia, M. Rossi, M. Benabadji, and N. Mohandas. 1986. Restoration of normal membrane stability to unstable protein 4.1-deficient erythrocyte membranes by incorporation of purified protein 4.1. *J. Clin. Invest.* 78:80–85.

Tolomeo, J. A., C. R. Steele, and M. C. Holley. 1996. Mechanical properties of the lateral cortex of mammalian auditory outer hair cells. *Biophys. J.* 71:421–429.

Ungewickell, E., and W. Gratzer. 1978. Self-association of human spectrin. A thermodynamic and kinetic study. *Eur. J. Biochem.* 256:7034–7039.

Waugh, R., and E. A. Evans. 1979. Thermoelasticity of red blood cell membrane. *Biophys. J.* 26:115–131.

Waugh, R. E., and P. Agre. 1988. Reductions of erythrocyte membrane viscoelastic coefficients reflect spectrin deficiencies in hereditary spherocytosis. *J. Clin. Invest.* 81:133–141.

Weaver, F. E., H. Polster, P. Febboriello, M. P. Sheetz, H. Schmid-Schonbein, and D. E. Koppel. 1990. Normal band 3-cytoskeletal interactions are maintained on tanktreading erythrocytes. *Biophys. J.* 58: 1427–1436.

Yuan, Y., and D. Axelrod. 1994. Photobleaching with a subnanosecond laser flash. *J. Fluor.* 4:141–151.